ADVANCED MATERIALS
www.advmat.de

Atomic Layer Deposition for Membranes, Metamaterials, and Mechanisms

Kyle J. Dorsey, Tanner G. Pearson, Edward Esposito, Sierra Russell, Baris Bircan, Yimo Han, Marc Z. Miskin, David A. Muller, Itai Cohen, and Paul L. McEuen**

Bending and folding techniques such as origami and kirigami enable the scale-invariant design of 3D structures, metamaterials, and robots from 2D starting materials. These design principles are especially valuable for small systems because most micro- and nanofabrication involves lithographic patterning of planar materials. Ultrathin films of inorganic materials serve as an ideal substrate for the fabrication of flexible microsystems because they possess high intrinsic strength, are not susceptible to plasticity, and are easily integrated into microfabrication processes. Here, atomic layer deposition (ALD) is employed to synthesize films down to 2 nm thickness to create membranes, metamaterials, and machines with micrometer-scale dimensions. Two materials are studied as model systems: ultrathin SiO_2 and Pt. In this thickness limit, ALD films of these materials behave elastically and can be fabricated with f)-scale bending stiffnesses. Further, ALD membranes are utilized to design micrometer-scale mechanical metamaterials and magnetically actuated 3D devices. These results establish thin ALD films as a scalable basis for micrometer-scale actuators and robotics.

Scaling and Moore's law have guided the miniaturization of transistors for 50 years: device dimensions are decreased proportionally such that the electric field E remains constant. The most challenging scaling dimension is the gate oxide thickness t, and atomic layer deposition (ALD) was invented as a means to create nanometer-thick gate oxides with excellent dielectric properties. The analogous scaling parameter for a thin flexible mechanical system is the strain field ε, with the same challenge of making nanometer-thick, high-quality layers. Constant-strain scaling is used to design mechanical systems derived from bending and folding such as deployable spacecraft solar panel arrays,[1,2] soft robots,[3–6] stents,[7] mechanical metamaterials,[8–11] and microelectromechanical systems.[12–16] We show that ALD is an ideal approach for scaling mechanical systems to micrometer-scale dimensions. In particular, the cycle-by-cycle thickness control and low defect density offered by ALD enables precise and reproducible design of mechanical systems while retaining integration with standard microfabrication considerations. These features of the ALD process are especially important at the nanometer scale, where films produced by other methods such as sputtering and evaporation are discontinuous, rough, or islanded. Our work demonstrates that free-standing ALD films with nanometer dimensions can be produced at high yield, be released from their substrate with mechanical integrity, and be shaped into micromechanical devices.

We have developed an entire fabrication strategy, including lithography, etching, release, and integration. The ALD films are grown conformally on a sacrificial layer of aluminum, as shown schematically in **Figure 1**a. The devices consist of lithographically patterned regions of ALD membranes and thicker panels of other materials that provide rigid structure and additional functions such as mirrors or magnets. X-ray reflectometry (XRR) and cross-sectional scanning transmission electron microscopy (STEM) are used to determine the film thickness, as shown for ALD SiO_2 grown on Al_2O_3 in Figure 1c,d. The devices are fabricated at wafer scales (Figure 1b) at yields exceeding 90%. If we desire topographic structure in the ALD membrane, the sacrificial aluminum layer can be patterned and anisotropically etched prior to film growth. Additional photolithography and deposition define reflective metals for optical elements and ferrous metals for magnetic elements. A negative photoresist polymer (see the Experimental Section) is used both for rigid panels in the designs and also as a stress-relief mechanism for the evaporated metals. Finally, the wafer is diced and devices are released by immersing in dilute base, followed by

K. J. Dorsey, T. G. Pearson, B. Bircan, Dr. Y. Han, Prof. D. A. Muller
School of Applied and Engineering Physics
Cornell University
271 Clark Hall, Ithaca, NY 14853, USA

E. Esposito, Prof. M. Z. Miskin,[+] Prof. I. Cohen, Prof. P. L. McEuen
Laboratory of Atomic and Solid State Physics
Cornell University
511 Clark Hall, Ithaca, NY 14853, USA
E-mail: itai.cohen@cornell.edu; plm23@cornell.edu

S. Russell
College of Nanoscale Sciences
SUNY Polytechnic Institute
247 Fuller Road, Albany, NY 12203, USA

Prof. M. Z. Miskin,[+] Prof. D. A. Muller, Prof. I. Cohen, Prof. P. L. McEuen
Kavli Institute for Nanoscale Science
Cornell University
420 Physical Sciences Building, Ithaca, NY 14853, USA

The ORCID identification number(s) for the author(s) of this article can be found under https://doi.org/10.1002/adma.201901944.

[+]Present address: Department of Electrical and Systems Engineering, University of Pennsylvania, 203 Moore Building, Philadelphia, PA 19104, USA

DOI: 10.1002/adma.201901944

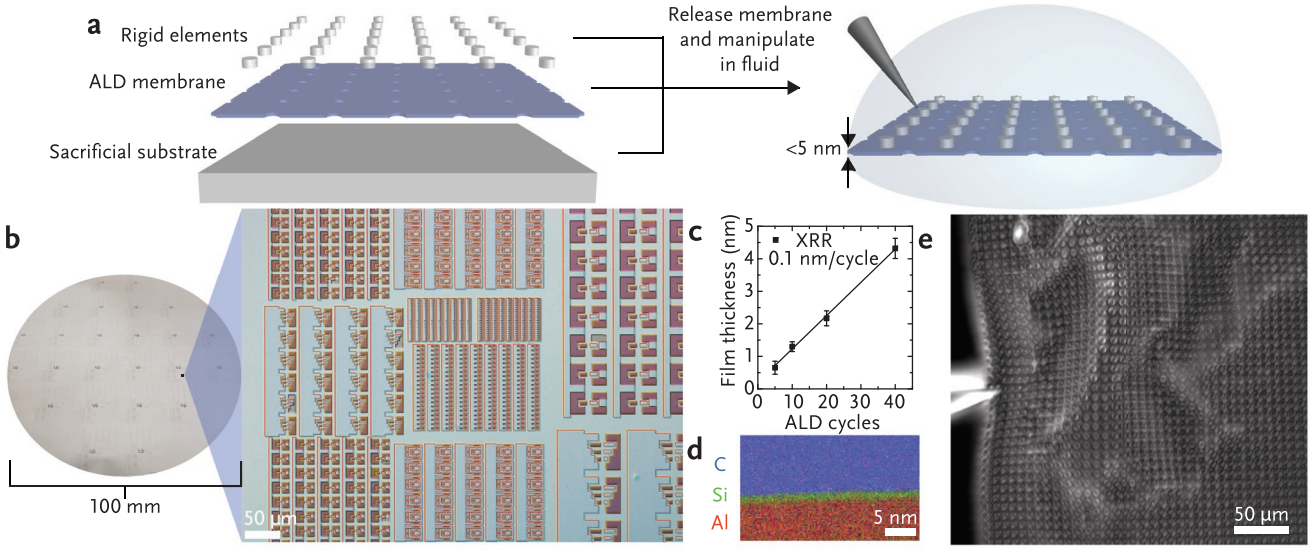

Figure 1. Fabrication and characterization of releasable ALD membranes. a) ALD devices consist of rigid elements (panels, mirrors, and magnets) deposited on an ALD membrane on a sacrificial film of aluminum. The aluminum is etched to release the devices. b) Photograph of a 100 mm wafer with myriad ALD devices. c) ALD thickness as inferred from XRR showing a constant thickness gain per cycle. d) Cross-sectional STEM of ALD SiO_2 grown for 20 cycles on an Al_2O_3 release layer. e) Focal plane projection of an ALD membrane crumpled by a micromanipulator probe.

rinsing in water. Upon release, all experiments are carried out in aqueous environments, often with added surfactant, to avoid stiction of the free membranes.

The sheet shown in Figure 1e is a 5 nm thick membrane of SiO_2 with visualization markers being crumpled with a micromanipulator probe. Upon release of the probe, the sheet returns to its original geometry. This can be repeated multiple times without degradation of the membrane. The 3D position of each marker is tracked by focal plane scanning, enabling calculation of the film curvature and therefore the strain field. From an analysis of the image, we estimate that the maximum strain ε in the film is 10^{-3}.

To measure the bending stiffness of such films, we use arrays of singly clamped cantilevers ($L \gg W$, $t = 5$ nm), with varying lengths and widths with metal pads patterned at their ends and polymer visualization markers along their lengths (**Figure 2**a,b). We apply forces to the metal pads with the radiation pressure from an infrared laser and measure the deflections by adjusting the focus of a piezo-controlled microscope objective.[17] A force–distance curve (Figure 2c) is shown for a representative device (10 μm × 100 μm). The fitted spring constant for this cantilever is 1.4×10^{-7} N m^{-1}, over eight orders of magnitude softer than typical atomic force microscopy cantilevers. This cantilever was actuated reversibly for 500 cycles with no signs of plastic deformation.

The spring constant is related to its bending stiffness through $k = 3\kappa W/L^3$, where W is the cantilever width and L is the cantilever length. Spring constants for devices of varying geometry are summarized in Figure 2d, normalized by the width. The spring constants show scaling consistent with a single bending stiffness $\kappa = 0.8 \pm 0.1$ fJ. This value for the bending stiffness is comparable to values obtained for wrinkled graphene.[17]

We also measured the bending stiffness of over 60 hinges ($W \gg L$), in this case actuated magnetically (Figure 2e–g). Ferromagnets with a saturated in-plane moment μ_s are deflected when we apply an out-of-plane magnetic field B. The bending moment on a hinge with dimensions $L \times W$ is given by $\tau_{hinge} = \kappa\theta(W/L)$. This must equal the magnetic torque $\tau_{mag} = |\mu \times \mathbf{B}| = \mu_s B \cos\theta$, yielding: $\theta/\cos\theta = \mu_s B/\kappa(W/L)$.[18] We test this relationship by fabricating hinges schematically drawn in Figure 2e. A 1 μm thick panel is patterned on top of the magnet which serves a dual purpose of managing residual thin-film stress in the magnet layer and as a spacer layer to control magnetic interactions between different parts of the device. The magnetic moment and coercivity of the magnetic film were measured by vibrating sample magnetometry (Figure S4, Supporting Information). Figure 2f shows the measured hinge deflection angles for ALD films of two different thicknesses, 5 and 8 nm, as a function of the magnetic field B. (Initial deflections of the hinge are taken into account in the term θ_0.) The hinge is deflected reversibly with no observable hysteresis (Figure 2f). Similar data were obtained for a 2 nm SiO_2 film, which is presented in Figure S1 in the Supporting Information. The behavior agrees well with the predicted magnetic moment/torque relation.

This experiment is repeated on 65 hinges with three different film thicknesses (2, 5, and 8 nm) to infer the bending stiffness. The bending stiffness is related to the Young's modulus Y and Poisson's ratio ν of the material through $\kappa = Yt^3/12(1-\nu^2)$. We fit this equation to the stiffness of each hinge as a function of thickness in Figure 2g. Scaling the thickness from 2 to 8 nm results in nearly two orders of magnitude change in the bending stiffness. Power-law stiffness scaling and angstrom-scale thickness precision of ALD enable precise bending stiffness engineering. We extract the Young's modulus of SiO_2 from the fit in Figure 2g, finding $Y = 90 \pm 10$ GPa. This value is comparable to values for bulk material (70–80 GPa), indicating that even at 2 nm thickness, the films behave mechanically similar to macroscopic counterparts. We operate these hinges

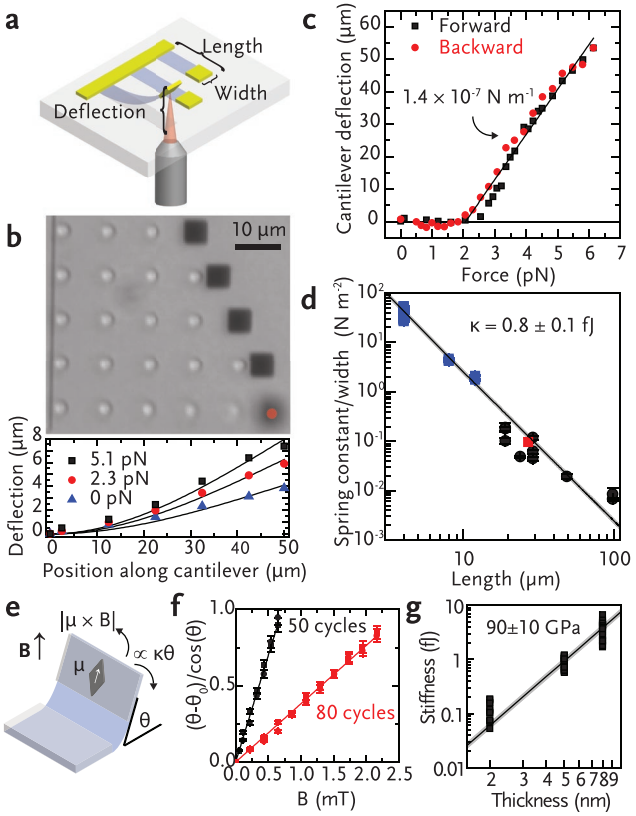

Figure 2. Mechanical properties of ALD membranes. a) Schematic drawing of the radiation-pressure force–distance measurement. b) Transmission optical microscopy image of polymer-decorated cantilevers. The beam profile can be reconstructed from the positions of the dots. c) Force–distance curve for a cantilever with $W = 10\,\mu m$, $L = 100\,\mu m$, and $t = 5\,nm$. The weight of the pad keeps the cantilever from deflecting for small applied forces. d) Compilation of spring constants as a function of cantilever geometry, showing consistency with a single bending stiffness for $t = 5\,nm$. Black circles correspond to optical pressure measurements, red square corresponds to a gravity-based measurement, and blue squares correspond to magnetically actuated measurements. e) Schematic of the applied and restoring torques for a magnetically actuated hinge. f) Forward and backward field sweeps for two magnetically actuated hinges fabricated from 5 and 8 nm films. Square markers are forward sweeps and circular markers are reverse sweeps. g) Measured hinge stiffness for SiO_2 films of 2, 5, and 8 nm thickness.

thousands of times without observation of failure (Video S1, Supporting Information) because extreme deformations are possible at low bending strain.

ALD membranes can readily be made into mechanical metamaterials through in-plane and out-of-plane patterning. **Figure 3** presents several example metamaterials that utilize lithography to engineer their properties. The sheet can become stretchable by cutting patterns that allow parts of the sheet to bend/buckle out of its fabrication plane.[19] For example, the pattern of cuts shown in Figure 3a connects the vertices of rigid triangular panels with soft flexible cantilever springs. As a probe stretches the metamaterial, it accommodates the strain by rotating and buckling the rigid panels off of the substrate. This is in dramatic contrast to the continuous membrane shown in Figure 1e which is unable to be significantly stretched. When the probe is returned to its initial position, the sheet returns to its original shape. The sheet can be stretched to nearly twice its original dimensions without failure, though the strains within the material remain below 10^{-3}. The panels can be fabricated from functional elements, such as reflective metals as we demonstrate in our device, to produce force-actuated optical elements at the micrometer scale.

A metamaterial with a negative Poisson's ratio, also known as an auxetic, is shown in Figure 3b.[20–23] This material is patterned from 5 nm thick sheet of ALD platinum (Figure 3b). Under application of an axial strain, the sheet expands in the transverse direction, yielding a negative Poisson's ratio as shown in Figure 3c. The Poisson's ratio only becomes positive when entire unit cells buckle out of the device plane.

Corrugated membrane metamaterials can also be created by patterning the substrate prior to ALD growth, as shown in Figure 3d–f. Corrugations parallel to the loading direction increase the bending stiffness while corrugations perpendicular to the loading direction remain flexible,[12,24] effecting anisotropic mechanical properties within a sheet. The alternating pattern of 75 nm deep parallel and perpendicular corrugations shown in Figure 3d allows the sheet to flex only where the corrugations are perpendicular; the parallel sections are nearly a thousand-fold stiffer than the perpendicular regions (see the Experimental Section). When the sheet is compressed (Figure 3e), it adopts an accordion-like buckled configuration. Periodic perforations in the sheet serve as a contrast agent making possible a 3D reconstruction of the buckled sheet (Figure 3f). Corrugated ALD membranes such as these can be used to create micrometer-scale origami devices with corrugated folds and panels that collapse into a desired final shape under compression or exhibit bistable behavior.[25–27]

These ultrathin materials can also be used for micrometer-scale actuators and machines that function with exquisitely small forces and torques. To demonstrate this concept, we present three classes of magnetically actuated systems in **Figure 4**. The first class consists of devices inspired by pop-up kirigami (Figure 4a,b). By placing magnets on any panel that we wish to be vertical, we can create pop-up 3D structures such as the staircase in Figure 4a. To control the magnetization direction, we initially saturate the magnets in the same direction with a large external field and subsequently manipulate the structures with sub-coercive fields. Figure 4b shows a related device, but with an additional magnet on the base of the structure. Continuous rotation of the external magnetic field can fold the structure over on top of itself at which point it forms a latch with the bottom magnet.

The devices shown in Figure 4c–e are magnetic actuators that contract to bear loads. The free end of a magnetically actuated cantilever bears a weight fabricated from platinum. If the restoring force of the cantilever exceeds the weight of the load, it lifts the weight off the substrate as in Figure 4c. On the other hand, if the weight exceeds the restoring force of the cantilever, it is dragged along the substrate (Figure 4d). Each weight panel exerts ≈2.4 pN of force on the end of the cantilever. We vary the number of weights on a cantilever of fixed geometry, measure its deflection, and calculate its mean curvature to produce a force–distance curve for the device. Despite the extreme deformations, this structure is still accurately described as a singly clamped cantilever with its boundary

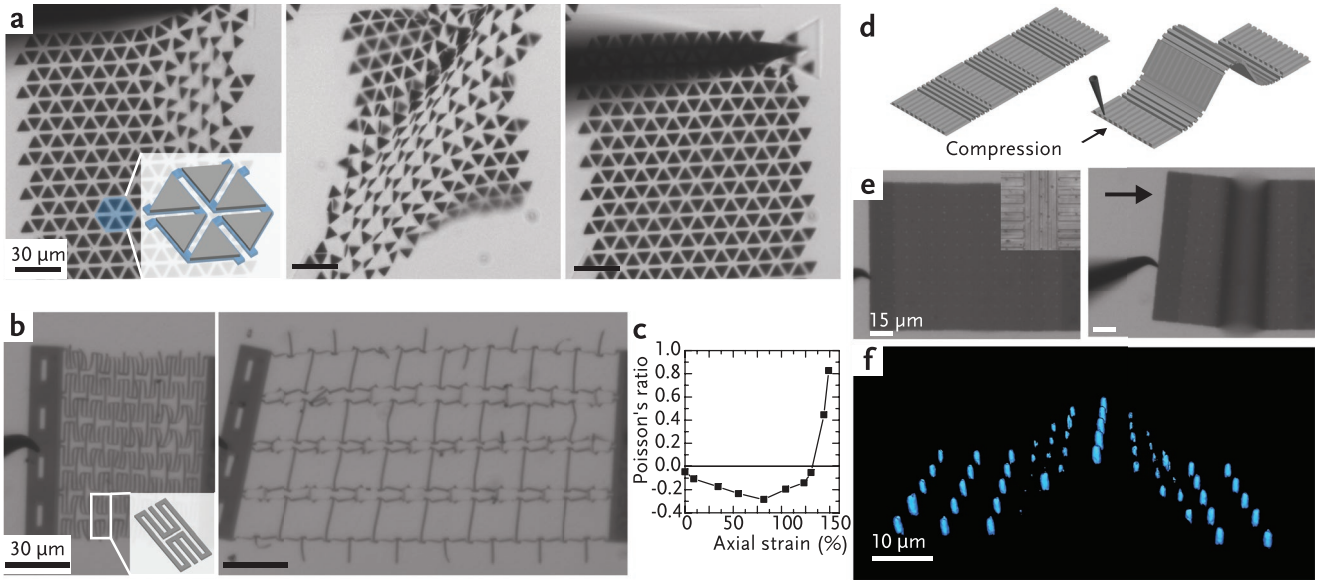

Figure 3. Mechanical metamaterials. a) Biaxially stretchable mechanical metamaterial. Rigid evaporated platinum triangles are connected by thin SiO_2 cantilevers that enable the sheet to be stretched and return to its original shape. b) Auxetic metamaterial patterned from ALD platinum. The re-entrant lattice expands as the sheet is stretched. c) Poisson's ratio for the auxetic sheet in (b). The Poisson's ratio remains negative for most of the spring's extension. d) Schematic of corrugated ALD membranes. The release layer it patterned with trenches which are transferred to the sheet upon release. e) Transmission optical image of a corrugated metamaterial of ALD platinum (inset: reflection optical image of corrugation pattern). Upon compression, the sheet only buckles where perpendicular corrugations have been patterned. f) 3D reconstruction of the buckled sheet from focal plane stacking with a piezo-controlled microscope objective showing the triangular buckled configuration.

condition set by the magnetic panel. For a cantilever with dimensions 10 μm × 27 μm, we calculate a spring constant $k = (9.5 \pm 0.1) \times 10^{-7}$ N m^{-1}, which is plotted in Figure 2d to show consistency with the other measurements. A related device is shown in Figure 4e, where magnetic panels are attached to linear springs. Upon application of an external field, the panels rotate out of the plane and move laterally closer to each other while applying a load on the springs in an analogous fashion to a muscle.

Finally, a gripper device is shown in Figure 4f. The gripper has magnets along the folding panels patterned as isosceles triangles to force the magnetization to spontaneously align along the median of the triangle. Application of a magnetic field forces the device to orient its panels along the field axis, producing a gripping motion.

The magnetically actuated structures and devices presented here demonstrate functional components of micrometer-scale machinery. Many envisioned applications of small machines involve deployment in inaccessible locations, such as within organisms.[14] Magnetic fields provide a useful external control mechanism as magnetic fields are not screened by tissue.[28] Our ALD-derived devices exploit the utility of magnetic control while opening the possibility for further scaling at shorter length scales. Furthermore, local control over the magnetic order within an elastic sheet enables shape-transforming soft robotics at the macroscale.[29–31] ALD sheets with magnetic panels with patterned magnetization enable realization of similar magnetic soft robots at the micrometer scale.

The mechanical properties and fabrication protocols for ALD membranes and metamaterials facilitate their potential application in very sophisticated micromechanical systems. For example, the low processing temperatures and fabrication compatibility enable ALD actuators to be added to silicon-based integrated circuits for smart microsystems and machinery. In addition, the diverse materials palate offered by ALD enables bimorph actuators of dissimilar materials while still maintaining a low bending stiffness for the film stack. These actuators can be leveraged to create self-assembled and environmentally responsive 3D structures and actuators. An additional benefit of ultrathin versions of bulk materials is that the surface chemistry of many ALD films is well-studied. This enables chemical functionalization and patterning, enabling the coupling between chemical sensitivity and mechanical responsivity. Combination of these capabilities may be used for sensors, self-assembled devices, optical devices, and microscale robotic systems.

Experimental Section

Device Fabrication: The devices presented in this paper were fabricated on piranha-cleaned Borofloat glass wafers. First, a layer of aluminum or 1% silicon in aluminum was deposited with thermal evaporation (Al) or DC sputtering with an radio frequency backsputter (Al/Si alloy) to a thickness of 300 nm to serve as a release layer for the ALD devices. Photolithography and reactive ion etching defined alignment markers in the aluminum which were used for all future process steps. Photolithography and BCl_3-based inductively coupled reactive ion etching defined trenches in the aluminum release layer for corrugated devices. The sidewall angle was 85°–88° as determined from scanning electron microscope. After these first two layers of lithography, wafers were cleaned in organic solvents and oxygen plasma to remove residues prior to ALD. The ALD was carried out in either an Oxford FlexAL plasma-assisted reactor at 200 °C (for metal oxides) or in an Arradiance thermal reactor at 250 °C (for platinum). Prior to growth of the ALD film of interest, 20 cycles of aluminum oxide were grown as a buffer layer to ensure a

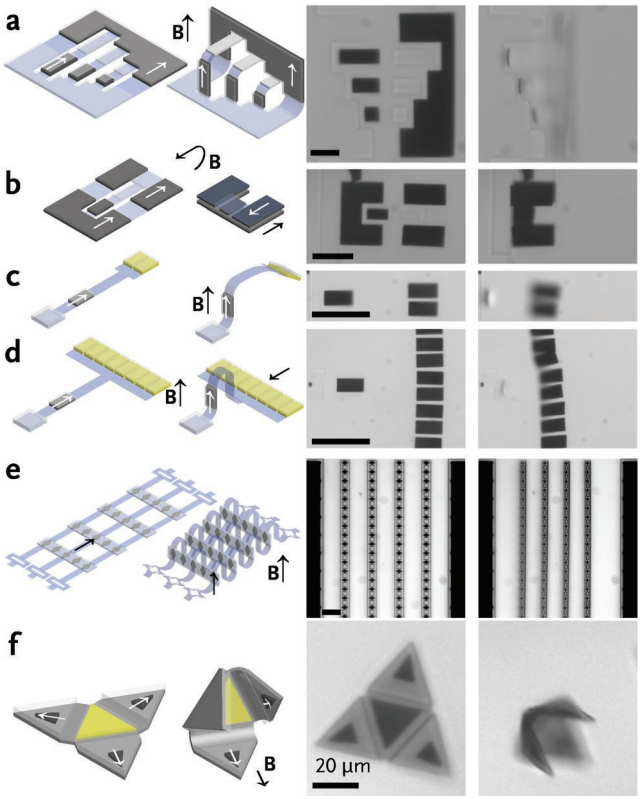

Figure 4. ALD-enabled magnetic mechanisms. a) Pop-up staircase actuated with external magnetic fields. b) A pop-up step integrated with a magnetic latch that folds the device flat when rotating the external field. c) A magnetic actuator capable of lifting its load. d) A magnetic actuator that produces linear actuation of its load. e) A magnetic actuator that applies forces to a spring. f) A magnetic gripper with radially oriented magnetization.

consistent surface chemistry for the device ALD. This buffer layer etched away during the device release. Tris[dimethylamino]silane and oxygen plasma were used for SiO_2 growth and trimethyl(methylcyclopentadienyl) platinum(IV) and O_2 were used for Pt growth. Photolithography, electron-beam evaporation, and liftoff were subsequently used to pattern metals. Additional photolithography and CF_4-based reactive ion etching (SiO_2) or argon ion milling (Pt) defined device geometry. Finally, either SU8 epoxy (MicroChem, 2000 series) or AZ nLOF photoresist (Microchemicals, 2000 series) was patterned to form device anchors, visualization aids, and stress-relief mechanisms. The devices were released in 2.38% tetramethylammonium hydroxide solution with added surfactants (1×10^{-3} M, sodium dodecyl benzene sulfonate). Perforations in the ALD sheet were optionally incorporated into our designs to adjust the release time. The etch selectivity between the ALD membrane and the release layer set an upper bound on the uninterrupted lateral dimensions of a sheet, because the largest lateral distance set the total release time. Therefore, designed were the largest lateral dimensions to be much less than the product of the sheet thickness times the selectivity to avoid damage to the ALD layer. For the sheets shown in Figure 1e, patterned were 2 µm diameter holes at 8 µm pitch to meet this condition. This was not a necessary step for the other reported structures.

ALD Film Characterization: Samples for cross-sectional STEM and electron energy loss spectroscopy (EELS) were prepared using focused ion beam (FIB) milling in an FEI Strata dual-beam FIB. To protect samples during this procedure, they were fabricated identically as the membranes under study, but with the addition of an amorphous carbon cap. Thin lamina were milled from the substrate and attached to a micromanipulator probe. The probe was then brought near a transmission electron microscopy grid, and the lamina was transferred from the probe to the grid. The sample was further thinned with a low-energy ion beam at grazing incidence. STEM and EELS were performed in an FEI Titan Themis STEM at 120 keV. The beam convergence angle was 30 mrad, with a probe current of ≈15 pA. The EELS spectrum and images were acquired with an energy dispersion of 0.25 eV per channel using a Gatan Quefina dual-EELS spectrometer. A linear combination of power laws was used to fit and subtract the background. The EELS false color composition map was created by integrating the silicon $L_{2,3}$ edge, the aluminum $L_{2,3}$ edge, and the carbon K edge. All of the EELS analyses were done with open source Cornell Spectrum Imager software. Images are included in Materials and Methods in the Supporting Information. As the sample was viewed in cross-section, the apparent layer width of a conformal layer was the true layer width blurred with the projected roughness from the substrate; thus, the imaged layer thickness should be viewed as an upper bound.

Mechanical Measurements of ALD Bending Stiffness: Forces applied to cantilevers using the radiation pressure were calculated by

$$F = \beta \frac{P}{c}(A + 2R) \tag{1}$$

where A is the absorbtion of the metal tag, R is the reflectivity of the metal tag, and β is an experimentally determined factor that accounts for the fraction of total applied power P that is incident on the tag. As the power was increased, the focal plane of the tag was tracked with a piezo-controlled microscope objective (60X, NA = 0.7). The fitted linear slope of the force–distance plot yielded the spring constant for the device. The factor β was determined ex situ by focusing the laser through pinholes of varying diameters while measuring the transmitted power. The metal tags studied in these experiments were fabricated from 10 nm Ti/50 nm Au. The reflectivity was measured to be 0.97 at 1064 nm with broadband spectral reflectance (Filmetrics F40-UV, 140–1100 nm). The high reflectivity at this wavelength allowed to neglect the absorption term when calculating the applied radiation force.

Stiffening of a Corrugated Sheet: The stiffness of a plate was proportional to the moment of inertia of the plate's cross-section. For a plate of width W and thickness t, the moment of inertia is $I_0 = Wt^3/12$. For a plate with a trench with depth z and trench width d such that $W = 2d$, the moment of inertia is

$$I = \frac{(d-2t)t^3 + 2tz^3}{3} + \frac{(d+2t)t^3}{12} + (d+2t)t\left(z + \frac{t}{2}\right)^2 - AC_\gamma^2 \tag{2}$$

with

$$A = 2tz + (d-2t)t \tag{3}$$

and

$$C_\gamma = \frac{2tz^2 + (d-2t)t^2}{2zd - 2(d-2t)(z-t)} \tag{4}$$

For this system, $t = 5$ nm, $z = 75$ nm, and $d = 4$ µm, giving a relative stiffening $I/I_0 \sim 950$.

3D Reconstruction of Corrugated Materials: Corrugated ALD membranes were fabricated with a pattern of perforations that serve a dual purpose of facilitating device release and providing bright spots in transmission microscopy to localize the sheet in the z-axis. A piezo-controlled microscope objective (PiezoSystem Jena, 60x, NA 0.7) was used to scan through focus while recording the piezo displacement. The image sequence was intensity-thresholded frame-by-frame and the piezo displacement was used to reconstruct the 3D rendering.

Supporting Information

Supporting Information is available from the Wiley Online Library or from the author.

Acknowledgements

This work was supported by NSF grant DMR-1435829, Air Force Office of Scientific Research (AFSOR) multidisciplinary research program of the university research initiative grant FA2386-13-1-4118, Cornell Center for Materials Research (CCMR) through NSF MRSEC program (DMR-1719875), ARO grant W911NF-18-1-0032, National Science Foundation (NSF) Major Research Instrumentation Award DMR-1429155, and the Kavli Institute at Cornell for Nanoscale Science. This work was performed in part at the Cornell NanoScale Science and Technology Facility (CNF), a member of the National Nanotechnology Coordinated Infrastructure (NNCI), which is supported by the National Science Foundation (Grant NNCI-1542081). The datasets generated during and/or analyzed during the current study are available from the corresponding author on reasonable request.

Conflict of Interest

The authors declare no conflict of interest.

Keywords

atomic layer deposition, kirigami, metamaterials, nanofabrication, NEMS

Received: March 27, 2019
Revised: May 3, 2019
Published online: May 30, 2019

[1] S. A. Zirbel, B. P. Trease, M. W. Thomson, R. J. Lang, S. P. Magleby, L. H. Howell, in *Micro- and Nanotechnology Sensors, Systems, and Applications VII*, (Eds: T. George, A. K. Dutta, M. S. Islam), Vol. *9467*, International Society for Optics and Photonics, Bellingham, WA, USA **2015**, pp. 94671C–1.
[2] S. A. Zirbel, R. J. Lang, M. W. Thomson, D. A. Sigel, P. E. Walkemeyer, B. P. Trease, S. P. Magleby, L. L. Howell, *J. Mech. Des.* **2013**, *135*, 111005.
[3] D. Rus, M. T. Tolley, *Nature* **2015**, *521*, 467.
[4] T. S. Shim, S.-H. Kim, C.-J. Heo, H. C. Jeon, S.-M. Yang, *Angew. Chem., Int. Ed.* **2012**, *51*, 1420.
[5] A. Rafsanjani, Y. Zhang, B. Liu, S. M. Rubinstein, K. Bertoldi, *Sci. Rob.* **2018**, *3*, eaar7555.
[6] S. Li, D. M. Vogt, D. Rus, R. J. Wood, *Proc. Natl. Acad. Sci. U. S. A.* **2017**, *114*, 13132.
[7] K. Kuribayashi, K. Tsuchiya, Z. You, D. Tomus, M. Umemoto, T. Ito, M. Sasaki, *Mater. Sci. Eng., A* **2006**, *419*, 131.
[8] Z. G. Nicolaou, A. E. Motter, *Nat. Mater.* **2012**, *11*, 608.
[9] K. Bertoldi, V. Vitelli, J. Christensen, M. van Hecke, *Nat. Rev. Mater.* **2017**, *2*, 17066.
[10] M. A. Dias, M. P. McCarron, D. Rayneau-Kirkhope, P. Z. Hanakata, D. K. Campbell, H. S. Park, D. P. Holmes, *Soft Matter* **2017**, *13*, 9087.
[11] Z. Liu, H. Du, J. Li, L. Lu, Z.-Y. Li, N. X. Fang, *Sci. Adv.* **2018**, *4*, eaat4436.
[12] N. T. Eigenfeld, J. M. Gray, J. J. Brown, G. D. Skidmore, S. M. George, V. M. Bright, *Adv. Mater.* **2014**, *26*, 3962.
[13] O. D. Supekar, J. J. Brown, N. T. Eigenfeld, J. C. Gertsch, V. M. Bright, *Nanotechnology* **2016**, *27*, 49LT02.
[14] J. Rogers, Y. Huang, O. G. Schmidt, D. H. Gracias, *MRS Bull.* **2016**, *41*, 123.
[15] J.-H. Na, A. A. Evans, J. Bae, M. C. Chiappelli, C. D. Santangelo, R. J. Lang, T. C. Hull, R. C. Hayward, *Adv. Mater.* **2015**, *27*, 79.
[16] M. Z. Miskin, K. J. Dorsey, B. Bircan, Y. Han, D. A. Muller, P. L. McEuen, I. Cohen, *Proc. Natl. Acad. Sci. U. S. A.* **2018**, *113*, 466.
[17] M. K. Blees, A. W. Barnard, P. A. Rose, S. P. Roberts, K. L. McGill, P. Y. Huang, A. R. Ruyack, J. W. Kevek, B. Kobrin, D. A. Muller, P. L. McEuen, *Nature* **2015**, *524*, 204.
[18] E. Iwase, I. Shimoyama, *J. Microelectromech. Syst.* **2005**, *14*, 1265.
[19] A. Rafsanjani, K. Bertoldi, *Phys. Rev. Lett.* **2017**, *118*, 084301.
[20] R. Lakes, *J. Mater. Sci.* **1991**, *26*, 2287.
[21] L. J. Gibson, M. F. Ashby, *Cellular Solids: Structure and Properties*, 2nd ed., Cambridge University Press, Cambridge, UK **1997.**
[22] L. Mizzi, K. M. Azzopardi, D. Attard, J. N. Grima, R. Gatt, *Phys. Status Solidi RRL* **2015**, *9*, 425.
[23] X. Ren, R. Das, P. Tran, T. D. Ngo, Y. M. Xie, *Smart Mater. Struct.* **2018**, *27*, 023001.
[24] K. Davami, L. Zhao, E. Lu, J. Cortes, C. Lin, D. E. Lilley, P. K. Purohit, I. Bargatin, *Nat. Commun.* **2015**, *6*, 1.
[25] N. P. Bende, A. A. Evans, S. Innes-Gold, L. A. Marin, I. Cohen, R. C. Hayward, C. D. Santangelo, *Proc. Natl. Acad. Sci. USA* **2015**, *112*, 11175.
[26] J. L. Silverberg, A. A. Evans, L. McLeod, R. C. Hayward, T. Hull, C. D. Santangelo, I. Cohen, *Science* **2014**, *345*, 647.
[27] B. Liu, J. L. Silverberg, A. A. Evans, C. D. Santangelo, R. J. Lang, T. C. Hull, I. Cohen, *Nat. Phys.* **2018**, *14*, 811.
[28] F. Ongaro, S. Scheggi, A. Ghosh, A. Denasi, D. H. Gracias, S. Misra, *PLoS One* **2017**, *12*, e0187441.
[29] M. Boncheva, S. A. Andreev, L. Mahadevan, A. Winkleman, D. R. Reichman, M. G. Prentiss, S. Whitesides, G. M. Whitesides, *Proc. Natl. Acad. Sci. U. S. A.* **2005**, *102*, 3924.
[30] W. Hu, G. Z. Lum, M. Mastrangeli, M. Sitti, *Nature* **2018**, *554*, 81.
[31] Y. Kim, H. Yuk, R. Zhao, S. A. Chester, X. Zhao, *Nature* **2018**, *558*, 274.

